

Experimental and computational characterization of designed and fabricated 50:50 PLGA porous scaffolds for human trabecular bone applications

Eiji Saito · Heesuk Kang · Juan M. Taboas ·
Alisha Diggs · Colleen L. Flanagan · Scott J. Hollister

Received: 14 July 2009 / Accepted: 3 May 2010 / Published online: 4 June 2010
© Springer Science+Business Media, LLC 2010

Abstract The present study utilizes image-based computational methods and indirect solid freeform fabrication (SFF) technique to design and fabricate porous scaffolds, and then computationally estimates their elastic modulus and yield stress with experimental validation. 50:50 Poly (lactide-*co*-glycolide acid) (50:50 PLGA) porous scaffolds were designed using an image-based design technique, fabricated using indirect SFF technique, and characterized using micro-computed tomography (μ -CT) and mechanical testing. μ -CT data was further used to non-destructively predict the scaffold elastic moduli and yield stress using a voxel-based finite element (FE) method, a technique that could find application in eventual scaffold quality control. μ -CT data analysis confirmed that the fabricated scaffolds had controlled pore sizes, orthogonally interconnected pores and porosities which were identical to those of the designed files. Mechanical tests revealed that the compressive modulus and yield stresses were in the range of human trabecular bone. The results of FE analysis showed potential stress concentrations inside of the fabricated

scaffold due to fabrication defects. Furthermore, the predicted moduli and yield stresses of the FE analysis showed strong correlations with those of the experiments. In the present study, we successfully fabricated scaffolds with designed architectures as well as predicted their mechanical properties in a nondestructive manner.

1 Introduction

Tissue engineering scaffolds have been studied as temporary templates for defects in the body to support loads, cell attachment and tissue regeneration. To enhance bone tissue integration into the constructs, scaffolds should have interconnected porous architectures for cell migration and blood vessel infiltration [1]. It is also necessary to have sufficient mechanical properties to match and support physiological loading, which degrade in a favorable manner to transfer load support to tissues during healing [2–4]. To fulfill these requirements, it is necessary to design and fabricate scaffolds with controlled porous architectures [5, 6].

Biodegradable porous bone scaffolds have been fabricated using several methods, including phase separation [7–10], particle leaching [5, 11, 12] and gas foaming [13]. These techniques can achieve high porosities ($\sim 90\%$) and large surface area for cell adhesion and tissue regeneration. These techniques further incorporate hydroxyapatite or bioactive glass to increase the scaffolds mechanical properties [14, 15]. However, due to their high porosity and thin walls between pores, they do not have sufficient mechanical strength to support bone defect loading [16]. Furthermore, the pores are randomly located, and their interconnectivities are not well controlled. Although the mean pore diameter and overall scaffold porosity can be

E. Saito · A. Diggs · C. L. Flanagan · S. J. Hollister (✉)
Department of Biomedical Engineering, University of Michigan,
Ann Arbor, MI 48109, USA
e-mail: scottho@umich.edu

H. Kang · S. J. Hollister
Department of Mechanical Engineering, University of Michigan,
Ann Arbor, MI 48109, USA

S. J. Hollister
Department of Surgery, University of Michigan, Ann Arbor,
MI 48109, USA

J. M. Taboas
Department of Orthopedics Surgery, University of Pittsburgh,
Pittsburgh, PA 15219, USA

controlled by changing fabrication parameters like porogen diameters, it is impossible to precisely control pore location, pore diameter, pore interconnectivity, wall thickness, and wall location [17]. Therefore, the internal pore architectures of those scaffolds cannot be designed.

To fabricate designed scaffolds with higher mechanical properties and interconnected pores, researchers have studied solid freeform fabrication (SFF) methods with various rapid prototyping (RP) machines, such as stereolithography (SLA) [18], selective laser sintering (SLS) [19, 20], fused deposition molding (FDM) [21, 22] and 3D printing [23]. These techniques enable fabrication of scaffolds with a high mechanical modulus and well interconnected pore structures compared to the aforementioned techniques of porogen leaching, gas foaming and phase separation. Although SFF techniques expand the capability of fabrication of designed scaffolds, only a limited numbers of materials can be used due to their temperature limitation, or chemical cross linking methods [24].

To address these limitations, indirect SFF technique is another unique and versatile technique using inverse molding to cast custom scaffolds [25]. In this technique, the inverse molds of the desired scaffold shapes are fabricated using RP machines, such as SLA or other 3D printing machines. These secondary molds are then cast into the desired polymer or polymer solution. This technique has increased the material choices of scaffolds with various synthetic biodegradable polymers, including poly lactic acid (PLA) [26], poly glycolic acid (PGA) [25], poly propylene fumerate (PPF) [27, 28], poly ϵ -carprolactone (PCL) [29] and a composite of poly (propylene fumerate)/tricalcium phosphate (PPF/TCP) [30, 31].

Poly (lactide-*co*-glycolide acid) (PLGA) is a FDA approved biodegradable material [32] and has been widely studied both in vitro and in vivo. Many previous studies have shown low mechanical properties for load bearing purposes [5, 6, 13, 33–36]. Although some researchers achieved high compressive moduli, about 40–400 MPa, their scaffolds are still not well controlled for pore size and porosity [11, 37, 38]. We postulate that PLGA porous scaffolds can be fabricated using indirect SFF technique with controlled internal architectures and compressive modulus for load bearing sites.

A critical need for scaffold engineering is the ability to a priori design scaffolds for desired effective properties, to non-destructively assess how closely the fabricated scaffold compares to its design and to investigate if differences between designed and fabricated properties can be determined from fabrication artifacts using computer aided design (CAD), computed tomography (CT) and finite element analysis (FEA) [19, 39]. Image-based design (IBD) techniques have been utilized to design scaffolds that mimic anatomical and physical properties of human bone

[40–42], and readily interface with indirect SFF technique to fabricate designed scaffolds. In addition, micro-computed tomography (μ -CT) has been utilized to assess the fabricated scaffolds architecture in a nondestructive manner [43, 44]. Subsequently, the μ -CT techniques have been combined with voxel-based FEA to estimate scaffold mechanical properties and compare with experimental mechanical properties [20, 45–48].

In this study, the porous scaffolds were designed by IBD and fabricated by indirect SFF technique to evaluate the ability to control scaffold architecture and mechanical properties. We hypothesized that designed 50:50 PLGA porous scaffolds could be fabricated using indirect SFF technique whose compressive moduli and yield stresses were within the range of the human trabecular bone. In addition, those mechanical properties could be computationally predicted from non-destructive μ -CT scans using voxel-based finite element (FE) method. To assess this hypothesis, we designed three porosities, 0, 50, and 70%, of porous scaffolds with orthogonally interconnected pores using IBD and fabricated these scaffolds from 50:50 PLGA scaffolds using indirect SFF technique. We then measured the porosities, pore size and strut diameter of the fabricated scaffolds using μ -CT. Compressive moduli and strength of three orthogonal directions were measured by mechanical testing. Voxel-based FE methods were used to simulate both the designed and the fabricated scaffolds in order to computationally obtain elastic moduli and yield stresses. These values were compared to the experimental elastic moduli and yield stresses.

2 Methods

2.1 Material

50:50 PLGA (lot D#01080, Inherent Viscosity = 0.61 dl/g) was purchased from Birmingham Polymers, Inc. (Birmingham, AL) and preserved in a container with desiccants at -20°C to prevent moisture buildup. The polymer was left at room temperature for 30 min before further processing.

2.2 50:50 PLGA solid cube fabrications

50:50 PLGA solid cubes (0% porosity) were fabricated in a customized polytetrafluoroethylene (PTFE) mold with 7×7 mm square holes. The Teflon mold was preheated in the oven for 30 min, and the polymer pellets were periodically added to the mold until the desired volume was achieved and heated in a vacuum oven at 170°C for 3.5 h. The cubes were cooled to 100°C for 0.5 h, and then to room temperature. After removing the Teflon mold, 50:50

PLGA cubes were trimmed to become 7 mm height. X, Y, Z orientations of the solid cubes were determined as shown in Fig. 1e.

2.3 50:50 PLGA porous scaffold fabrication

Porous scaffolds with interconnected pores were fabricated using the indirect SFF technique as previously described [25]. An image of each step is shown in Fig. 1a–d. First, two porous scaffold designs with 50 and 70% porosities were designed by IBD method using the interactive data language (IDL) software (Research Systems, Inc., Boulder, CO) [40]. The orthogonally interconnecting pores were generated as a unit cell and replicated to fill the cubic volume. The external shapes of scaffolds were designed into 7 mm cubic shapes which were filled with the designed unit cells containing pore and struts. The pore and strut sizes of each scaffold were 664 and 464 μm , respectively for the 50% porous scaffold, and 878 and 228 μm , respectively for the 70% porous scaffold. The IDL generated image-based designs of the scaffolds were converted into stereolithography (STL) format, then, sliced using Modelworks software (Solidscape, Inc., Merrimack, NH), and finally read by PatternMaster™ 3D printer (Solidscape, Inc., Merrimack, NH) to fabricate wax molds.

Our fabrication method for the HA molds have been reported previously [49, 50]. From our previous research, HA has been known to shrink during the sintering process, and we designed the HA secondary molds to account for this, by a scaling factor of 1.37 [25]. HA slurry was casted into the wax molds, cured in a nitrogen atmosphere

overnight under a fume hood for 1 day, and immersed in acetone to remove the wax molds. The HA molds were cyclically burned out in the furnace to remove the polymer binding the HA particles and then, sintered at 1,350°C.

The 50:50 PLGA polymer pellets were added to the PTFE molds with a square hole to fit the HA secondary mold. The HA molds were then placed into the PTFE mold containing the molten PLGA polymer, and pushed through until the HA molds reached the bottom of the PTFE mold in order to force the polymer to penetrate into the open pore networks of the HA molds. The remainder of the casting protocol is identical to the solid cube fabrication. The polymer scaffolds containing HA molds were ground with a hand-milling machine to expose the HA on the surface of the scaffolds and submersed in RDO (APEX Engineering Products Corp, Plainfield, IL) under fluid agitation to remove HA from the porous polymer scaffold. Every 1–1.5 h, the scaffold was blown with air to clean out residual HA. X, Y and Z directions of scaffolds were determined and marked (Fig. 1). After the HA was removed from the scaffolds, polymer scaffolds were washed with ethanol, dried and returned to the freezer.

2.4 Characterization of fabricated scaffold morphology and volume fraction

Determination of the fabricated scaffold morphology, pore sizes, pore interconnectivity and volume fraction was done using a MS-130 high resolution Micro-CT Scanner (GE Medical Systems, Toronto, CAN). All of the solid cubic, 50 and 70% porous scaffolds were scanned at a resolution

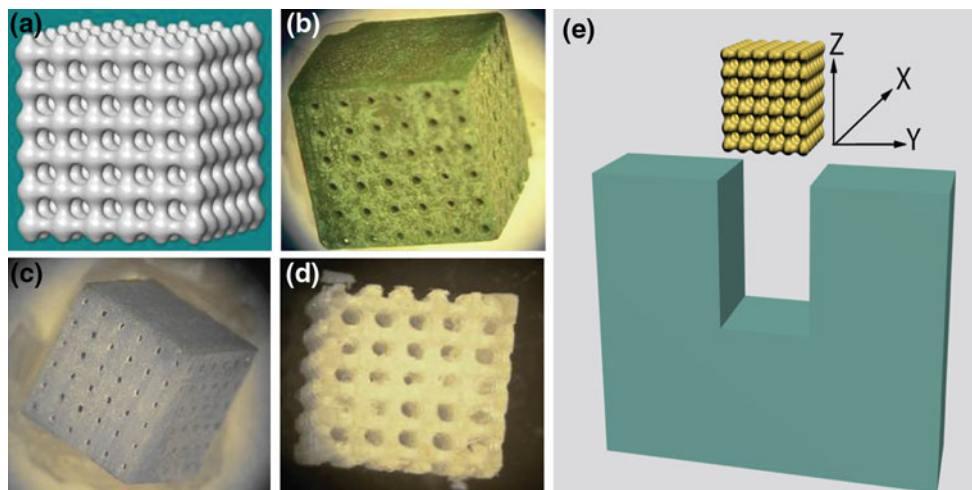


Fig. 1 Images of the scaffold fabrication process. **a** A porous scaffold was designed using IBD techniques and converted into stl file format. **b** A thermoplastic mold was fabricated using PatternMaster RP machine. **c** A hydroxyapatite secondary mold was cast into the thermoplastic mold followed by burning and sintering process. **d** 50:50 PLGA porous scaffold was cast into the HA secondary mold

and the HA mold was removed by RDO. **e** Orientation of the fabricated scaffolds. The orientations of the scaffolds were defined along to the casting directions. *Green color* represents one of the Teflon molds, and there are two Teflon plates attached both size in X direction. (Color figure online)

of 16 μm . The source volume was 75 kV and 75 mA and an aluminum filter was used. The scanned images were reconstructed using Microview software (GE Healthcare) and stored as .vff files. To determine the volume fraction of the scaffolds, the vff files were reoriented and output as .jpg files using Microview software. Finally, regions of interest (ROI) from the .jpg images were determined and converted to raw files, and the raw files were used to automatically calculate the fraction of volume using IDL software. The ROI was chosen to contain the entire scaffold, but not any area outside of the scaffold.

2.5 Mechanical testing

Compression tests were performed at a rate of 1 mm/min after a preload of 0.454 kg (1 lb) using a MTS Alliance RT30 Electromechanical test frame (MTS Systems Corp., MN). After scanning, all scaffolds were compressed to failure in one of three orthogonal directions (X, Y, Z) defined in the scaffold fabrication section. TestWorks4 software (MTS Systems Corp., MN) was used to record load and displacement data, and stress–strain curves were calculated from the initial dimensions of the specimens. The compressive modulus was defined by the slope at the initial linear section of the stress–strain curve. The yield stresses were calculated using the 0.2% offset method. One-Way ANOVA was performed using SPSS (SPSS, Inc., Chicago, IL USA), with significance defined as $P < 0.05$.

2.6 Finite element analysis of fabricated scaffold

The μ -CT scanned scaffolds were simulated using a voxel-based FE method to compare the compressive moduli with those of the experiments. The 3D .vff files were converted to Analyze format (.hdr) using the Microview software, and then imported into the ScanIP™ software (Simpleware Ltd., UK). The imported files were processed and exported into .stl formats. The stl files were imported into the voxel-based homogenization software, VOXELCON (Quint Corp, Tokyo, Japan), to create voxel, or equivalently 8-node hexahedral elements. The input moduli ($E_x = 2706.5$ MPa, $E_y = 2845.5$ MPa, $E_z = 2986.9$ MPa) were determined from the compressive tests of the solid cubes and Poisson's ratio of 0.3 was assumed for all models. The voxel size with 30 μm was applied to 50 and 70% porous scaffolds, and the voxel size with 50 μm was applied to the solid cubes. The uniaxial compressive loads in Z direction are applied to one side of the models, and the other sides were confined in Z direction. One voxel (not one node) of the constrained side was constrained with X and Y direction to prevent the rotation of the model. Convergence was achieved when the force and displacement residuals were $< 1 \times 10^{-4}$.

2.6.1 Prediction of modulus and yield stress of the designed porous scaffolds

Two loads were applied to the structure within the linear region of scaffold deformation. One was applied at the lower end of the linear region and one was applied at the upper end of the linear region. Since elastic modulus is linear, it could be determined from either applied load. The effective scaffold modulus was calculated as the slope of the applied stress (applied load/cross-sectional area) versus average strain (maximum displacement/initial length). To determine the yield stress of the designed scaffolds, the maximum stress of the voxels under each applied stress of the designed scaffold was calculated. Then, the relation between the applied stress and the maximum stress were plotted. Finally, the yield stress was determined at the point where the maximum stress reached value of the bulk yield stress.

2.6.2 Prediction of modulus and yield stress of the fabricated porous scaffolds

The effective moduli of the fabricated porous scaffold ($n = 9$) were calculated in the same way as the porous scaffold designs. For yield stress calculation ($n = 8$), cumulative histograms of von Mises stress distributions were plotted. Then, the histograms were fit to a modified cumulative Weibull function (Eq. 1) which includes two exponential terms.

$$f(x) = 1 - \left(p e^{-(x/\lambda)^{k_1}} + (1-p) e^{-(x/(r\lambda))^{k_2}} \right) \quad (1)$$

Where p is a weighting value for the exponential terms, k_1 and k_2 are the shape parameters, and λ and r are scale parameters of the fitting curve. The modified Weibull function was fit using the FMINCON optimization routine in MATLAB. After several tests, p values clustered around 0.1. Therefore, p was chosen as 0.1 in this study. k_1 , k_2 and r were found to be constant over the analyses for a scaffold regardless of the applied loads. It was also found that λ was proportional to the applied loads. Here, we introduced ε , a fraction of voxels having von Mises stress higher than the bulk yield stress (110 MPa from our experiments). For given p , k_1 , k_2 and r , λ at yield was determined for a given ε by Eq. 1. Also we calculated λ from bulk yield for given ε by direct relation in Eq. 1. Then, by interpolating two applied loads [high applied load (larger λ) and lower applied load (smaller λ)], we obtained the yield stress of the scaffold (Fig. 7b). Prediction was performed with various ε values (0.0001, 0.0003, 0.0005, 0.001, 0.002, and 0.003) and correlated to the experimental yield stresses.

3 Result

3.1 Assay of scaffold morphology

We designed and fabricated 18 of the 70% porous scaffolds, 16 of the 50% porous scaffolds and 25 solid cubes. As shown in Fig. 2a and d, the designs of porous scaffolds were composed of repeating unit cells with orthogonally interconnected pores in three directions and fitted to the desired outer dimensions of the porous scaffolds using the IBD technique. The three dimensional renderings of the fabricated scaffolds were obtained from the μ -CT data. The images revealed that the fabricated scaffolds (Fig. 2b, e) matched well with the designed architectures (Fig. 2a, d) and were composed of the repeated unit cells. Some cracks and undesired pores in the struts from the fabrication process were observed (Fig. 2c, f). Also, some residual hydroxyapatite was found inside of the scaffolds (data is not shown).

The volume fraction (inverse of porosity) was determined by taking the volume of polymer divided by total scaffold volume. The targeted volume fractions of 70 and 50% porous scaffolds and solid cubes were 30, 50 and 100% while the measured volume fractions were 23.6 ± 5.018 , 41.7 ± 4.558 , and $99.7 \pm 0.789\%$, respectively. The interconnected pore diameters and strut sizes adjacent to the pores were measured from the μ -CT images. The average measured pore and strut sizes [Designed pore and strut sizes are in brackets] were $807 \pm 49 \mu\text{m}$ [878 μm

and $296 \pm 48 \mu\text{m}$ [228 μm] for the 70% porous scaffolds, and $652 \pm 44 \mu\text{m}$ [664 μm] and $444 \pm 51 \mu\text{m}$ [464 μm] for the 50% porous scaffolds.

3.2 Mechanical properties of the fabricated porous scaffolds

The results of mechanical testing revealed that the compressive modulus and the yield stress varied depending on porosity of the scaffolds. The average modulus of the solid cube was obtained as $2851.9 \pm 133.5 \text{ MPa}$. 70% porous scaffolds and 50% porous scaffolds had achieved an average modulus of 89.5 ± 36.8 and $321.6 \pm 140.9 \text{ MPa}$, respectively. The average offset yield stress also changed depending on the porosity of the scaffolds. The values were 2.1 ± 1.2 , 10.3 ± 4.3 and $110.4 \pm 2.7 \text{ MPa}$ for 70% porous, 50% porous and solid cubes, respectively.

The anisotropy of the scaffold moduli and yield stresses were further examined (Fig. 3; Table 1). The results from the solid cube compressive moduli revealed that anisotropy was determined by casting orientation. The anisotropy of solid cubes showed the highest modulus in order of Z ($2986.9 \pm 35.8 \text{ MPa}$), Y ($2845.5 \pm 34.7 \text{ MPa}$) then, X ($2706.5 \pm 103.9 \text{ MPa}$) direction, and these were significantly different ($P < 0.05$). The results of the yield stresses showed only Y direction was significantly lower than Z direction. Although both compressive modulus and yield stress were slightly higher in Z direction of 70% porous

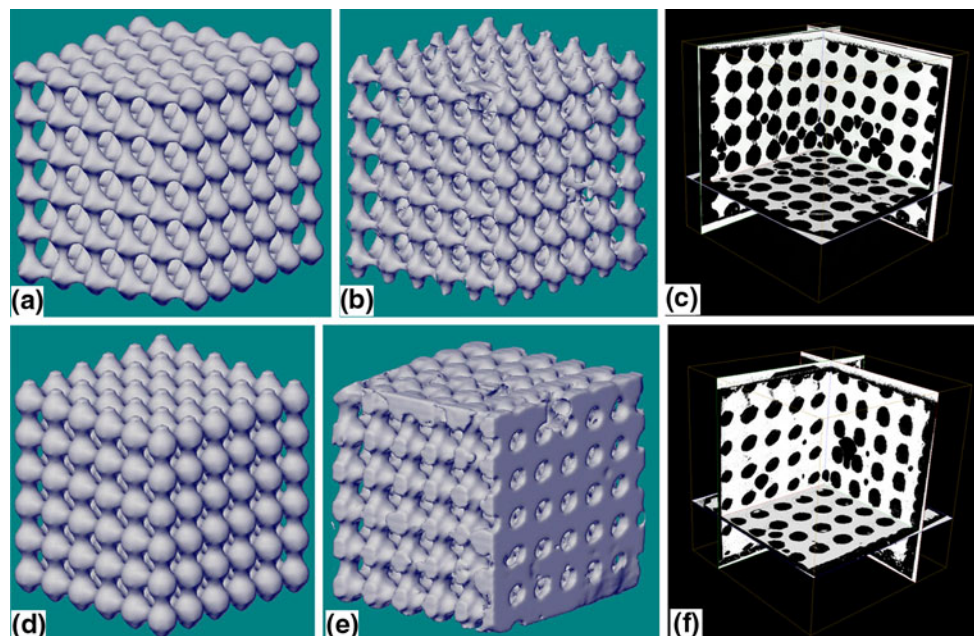


Fig. 2 Images of 50% porous 50:50 PLGA scaffold (a–c) and 70% porous scaffold (d–f). stl image of the designed scaffold (a, d). 3D rendering images of the fabricated scaffolds (b, e). μ -CT images of

fabricated scaffolds shows pore interconnectivity of fabricated scaffold and some defects inside of the scaffolds (c, f)

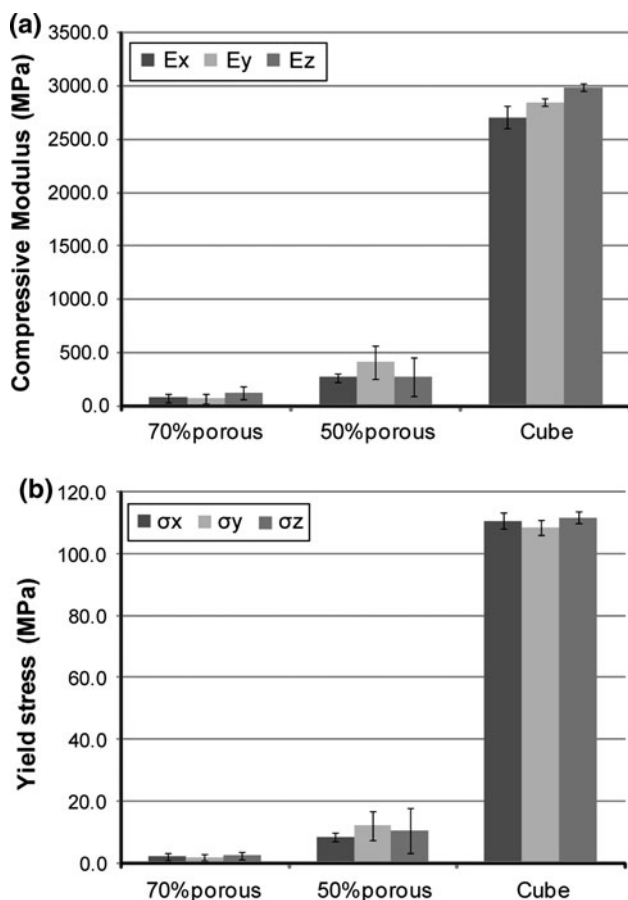


Fig. 3 Scaffold anisotropy in terms of compressive modulus (a) and yield stress (b). The value of compressive modulus and yield stress are shown in Table 1

scaffold and Y direction of 50% porous scaffold, the statistical results did not show any significant difference.

The mechanical test data of the 70 and 50% porous scaffolds were used to calculate the correlation between scaffold volume fraction and compressive modulus or yield stress depending on the scaffold test directions (Fig. 4). The compressive modulus result shows their linear relations and the regression values were 0.9061, 0.9002 and

0.8248 in all directions. These results show the porous scaffold modulus range could be varied from 50 to 500 MPa depending on the scaffold porosities. In addition, the yield stress showed a significant correlation in σ_x ($R^2 = 0.8397$) and σ_y ($R^2 = 0.8929$), but there is a weak relation in σ_z ($R^2 = 0.3327$).

3.3 Computational simulation of solid cubes and porous scaffolds

3.3.1 Stress distribution of the designed and fabricated scaffolds

Figure 5 shows that stress distributions in Z direction from the FE simulation within the range of linear elastic region of the scaffolds (1–2% strain). The different color shows the different stress levels where red indicates the highest tensile stress (50 MPa), blue indicates the highest compressive stress (–110 MPa) and yellow indicates zero stress (0 MPa). The designed porous scaffolds showed homogeneous stress in the Z direction (Fig. 5b, c), and higher stress concentrations appeared on the small struts on both designed porous scaffolds. The fabricated scaffolds demonstrated sporadic local compressive stress and tensile stress concentrations due to some casting defects in the scaffolds (Fig. 5e, f). Although there were minor stress concentrations on the fabricated scaffolds, the stress was distributed homogeneously on the entire model as the designed cube. The distributions of the stresses of the fabricated porous scaffolds were similar in both designed and the fabricated scaffolds.

Potential high stress concentrations in the fabricated scaffolds were also discovered using the FE simulation. Figure 6 shows an example to find the heterogeneous stress distribution of fabricated scaffolds. The scaffold was simulated with 50 N of loading which caused 1.85% strain deformation. Although this strain was within the elastic region and lower than the 0.2% offset yield strain from the experiment of this scaffold (2.53%), the stress on some

Table 1 Compressive modulus and yield stress of the scaffolds with three orthogonal directions

		X	Y	Z
70% Porous scaffold	N	6	6	6
	E (MPa)	77.6 ± 40.7	69.5 ± 41.5	121.6 ± 58.4
	σ (MPa)	2.1 ± 1.3	1.7 ± 1.0	2.5 ± 1.2
50% Porous scaffold	N	6	6	4
	E (MPa)	267.7 ± 39.5	407.7 ± 156.9	273.2 ± 178.4
	σ (MPa)	8.4 ± 1.5	12.1 ± 4.6	10.5 ± 7.3 (N = 3)
Solid cube	N	8	8	9
	E (MPa)	2706.5 ± 103.9	2845.5 ± 34.7	2986.9 ± 35.8
	σ (MPa)	110.7 ± 2.6	108.4 ± 2.4	111.8 ± 2.0

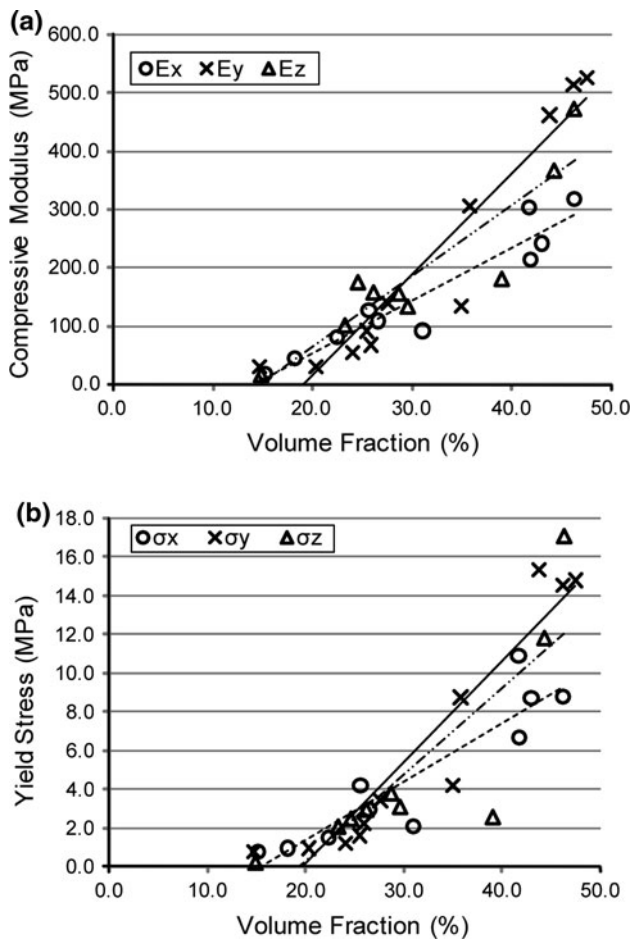


Fig. 4 Correlation of scaffold volume fraction with compressive modulus (a) and yield stress (b). The linear fitting curves are: dotted lines (Ex and σ_x), solid line (Ey and σ_y), and dashed dotted line (Ez and σ_z)

struts were equal to that of the yield value. In addition, there are some red color regions which indicate tensile stresses on the areas.

3.3.2 Prediction of compressive moduli and yield stresses of designed scaffolds

The predicted compressive moduli of the 50 and 70% porous scaffold designs determined from FE results were 553 and 173 MPa, respectively. Further prediction of the yield stress can be performed using the relation between applied stress and scaffolds maximum stress (Fig. 7a). The predictions of the yield stresses were determined at the point where the maximum stress of a voxel reaches 110 MPa (bulk yield stress from the experiment). The 50 and 70% porous scaffold designs reached the yield stress level when 10.76 and 2.94 MPa were applied, respectively.

3.3.3 Prediction of moduli and stresses of fabricated scaffolds

The simulation results show the average modulus of the solid cubes were 2646 ± 36 MPa ($n = 4$) and similar to that of the designed cube (2,707 MPa) and approximately 90% of the modulus of compression tests. The moduli of the fabricated scaffolds were also calculated from the FE results and compared with the experimental data (Fig. 8a). Although the simulated values were generally lower than those of the experiments, there was a significant correlation between the simulation and the experiments of fabricated porous scaffolds ($R^2 = 0.951$, $y = 1.6557x - 44.076$).

Fig. 5 The Z-stress distributions of simulated scaffolds in the linear elastic regions (1–2% strain): **a** designed cube, **b** designed 50% porous scaffold, **c** designed 70% porous scaffold, **d** fabricated cube, **e** fabricated 50% porous scaffold, and **f** fabricated 70% porous scaffold. **g** Scale bar of the stress ranges are –110 MPa (blue) to 50 MPa (red), and the yellow shows around 0 Pa stress. (Color figure online)

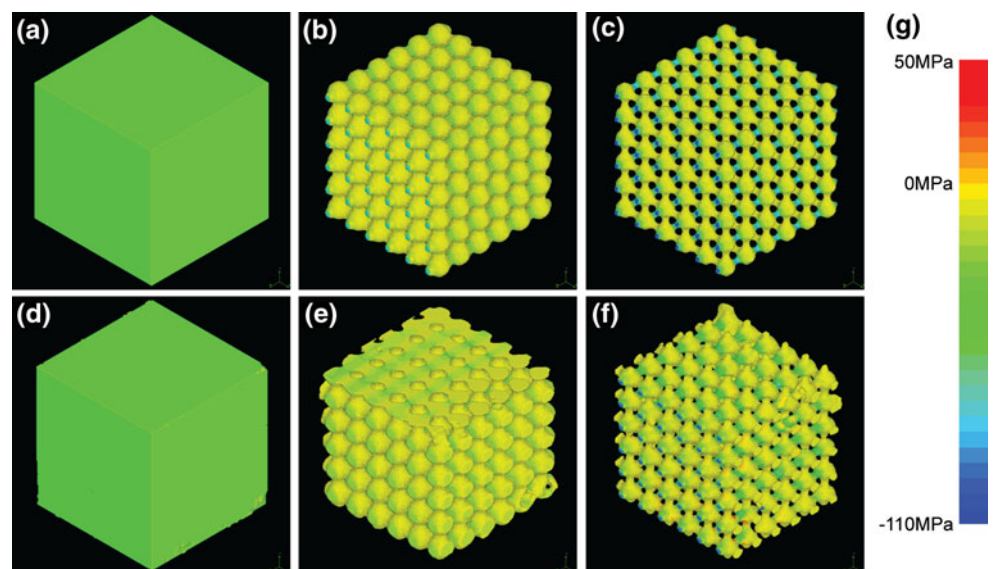
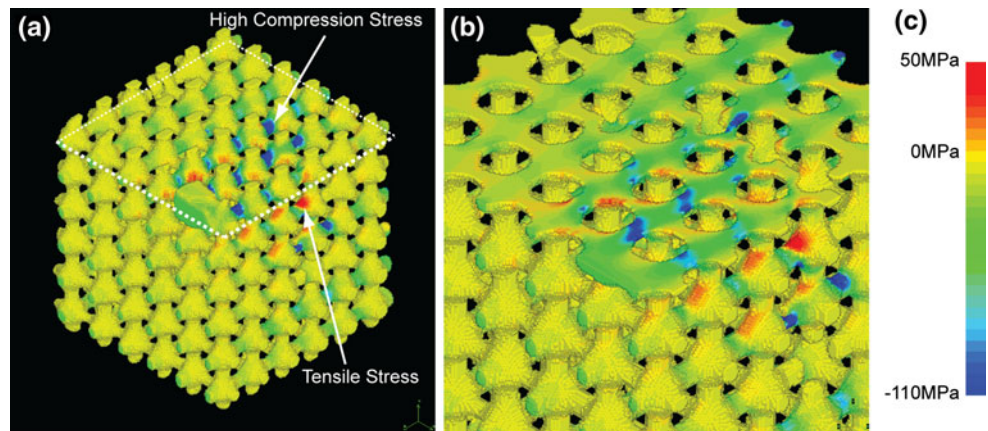


Fig. 6 The stress distribution of fabricated 70% porous scaffolds under 50 N loading which caused 1.85% strain. **a** The stress distribution of the entire scaffold. **b** The stress distribution of the cross section of the *white dot line*. The *blue colors* show the high stress region which may cause yield of the scaffold. **c** Scale bar of the stress ranges are -110 MPa (*blue*) to 50 MPa (*red*), and the yellow shows around 0 Pa stress. (Color figure online)



Yield stress of actual fabricated scaffolds was estimated using the modified Weibull function fitting. Figure 7b shows that the relation between the fraction of the voxels and their stress levels. The cumulative fraction of voxels at a given von Mises stress was fit well with the modified Weibull distribution. As applied loads increase, λ , σ and ε increase. When λ is smaller than λ_y ($\lambda = \lambda_L$), σ is smaller than σ_y ($\sigma = \sigma_1$), and the scaffold does not yield. When λ is bigger than λ_y ($\lambda = \lambda_H$), σ is bigger than σ_y ($\sigma = \sigma_H$), and the scaffold already yields. ε for yield stress was determined for a von Mises stress of 110 MPa. Under the yield strain, more than 99% of voxels have a stress level lower than the material yield stress (110 MPa). However, the simulation of the higher stress levels shows that the curves shift towards a lower fraction and indicate that more voxels are exposed to higher stress. Although various values of ε were applied, plots and linear fittings for only the minimum and maximum of ε are shown in Fig. 8b. For the tested ε range, the R^2 changed from 0.941 ($y = 0.7755x + 0.154$) to 0.946 ($y = 0.9062x + 0.4012$) with $\varepsilon = 0.001$ the highest which is also shown in Fig. 8b.

4 Discussion

Controlling pore diameter and porosity of the scaffolds is necessary to control mechanical properties as well as tissue regeneration and scaffold degradation [37]. We successfully fabricated 50:50 PLGA scaffolds with designed strut sizes, pores sizes and porosities using IBD and indirect SFF techniques, and those were analyzed using μ -CT. The scaffold outer shapes were designed in 7 mm cubical shape to mimic the trabecular bone samples commonly used to test mechanical properties [51]. To examine the effect of direction of casting on mechanical properties for the same specimen, the scaffolds with 1:1 ratio were examined instead of 2:1 ratio in the ASTM standard. The pore sizes of the scaffolds were designed similar or smaller compared

to other SFF scaffolds for bone application [20, 21]. Although the scaffolds have lower porosities, 50 and 70%, than the conventional scaffolds made by salt leaching and gas forming techniques, they have defined orthogonally interconnected pore architectures to allow mass transport into the scaffolds. In addition, lowering scaffold porosity may necessary to achieve high mechanical properties since the bulk property of this material is lower than bone.

Solid cubes were fabricated to find the best casting condition for porous scaffolds, and to obtain bulk material properties under our manufacturing conditions. The fabricated cubes had high volume fraction, and the bulk moduli and yield stresses which were much higher than those of trabecular bone [16, 52, 53], providing an upper bound on the attainable mechanical properties for porous scaffolds. The anisotropy of the mechanical properties may be explained that the fabrication process changed the polymer structures, such as crystallinity changes from differential scanning calorimetric tests (data not shown).

From the μ -CT data, it was confirmed that the pores of the 50 and 70% porous scaffolds were orthogonally interconnected and that the molten polymers successfully penetrated into the HA secondary mold to form the internal architectures. The pore and strut sizes of the fabricated scaffolds were close to the designed ones, but the fabricated scaffolds had 8–10% lower volume fractions, or higher porosity, than the designed values due to some defects or air bubbles trapped inside of the scaffolds. However, this difference was still smaller than those reported for early applications of direct SFF techniques, such as SLA (15–20%) [18]. Indirect SFF scaffolds made of PPF [27] also exhibited a larger deviation in volume fraction from designed ones. Compared with the previous scaffolds made by SFF techniques, the fabricated scaffolds had the same or better accuracy.

From the mechanical properties of both the 50% and 70% porous scaffolds, we obtained varying scaffold compressive moduli and yield stresses within the range of

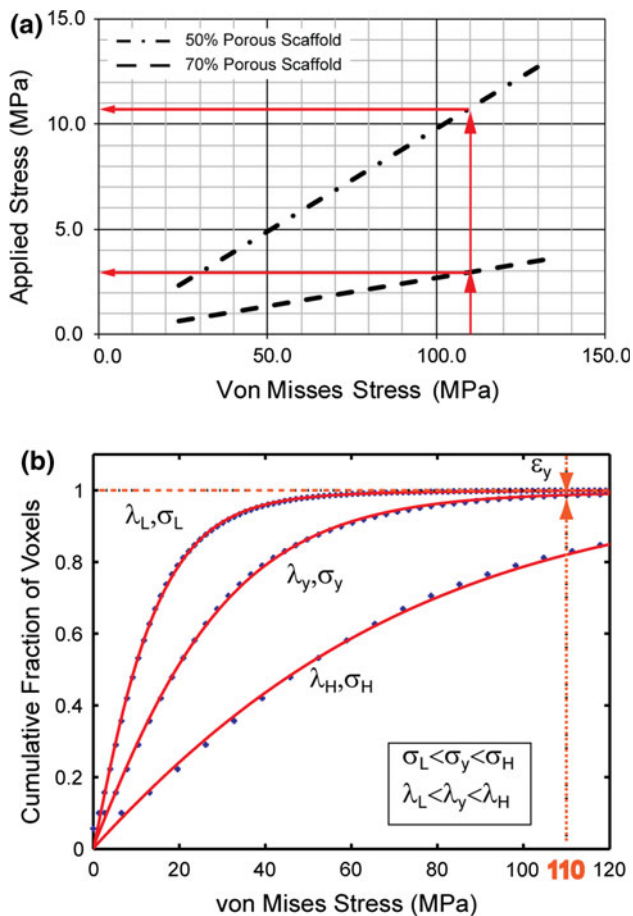


Fig. 7 The prediction of the yield stress from the simulation of the scaffold designs, 50% porous scaffold and 70% porous scaffold (a). The relation among Weibull fittings, σ and λ (b). When the scaffold does not yield, σ and λ are smaller than the σ_y and λ_y . ϵ is smaller than ϵ_y or equal to 0. When the scaffold yields, σ and λ are larger than the σ_y and λ_y . ϵ is bigger than ϵ_y

human trabecular bone, whose compressive modulus ranges from 10 to 900 MPa and yield stress from 0.2 to 14 MPa [16, 52, 53]. Our indirect SFF scaffolds also achieved higher compressive modulus and yield stress than scaffolds made by previous porogen leaching, phase separation and the composite techniques. In addition, 70% porous scaffold showed similar or higher modulus than other direct SFF techniques, such as 20–140 MPa of PPF scaffolds [18], 51.6 MPa of blended PCL/PLGA/TCP scaffolds [54] and 30–42 MPa of PCL scaffolds [21], although this is in part due to different bulk mechanical properties. The relation between the porosity of scaffolds and the mechanical properties showed increasing scaffold volume fraction increased the compressive modulus and yield stresses, consistent with other studies [5, 11, 23]. Furthermore, the mechanical properties of porous scaffolds are determined not only by their porosities but also by their architectures, including pore sizes and strut

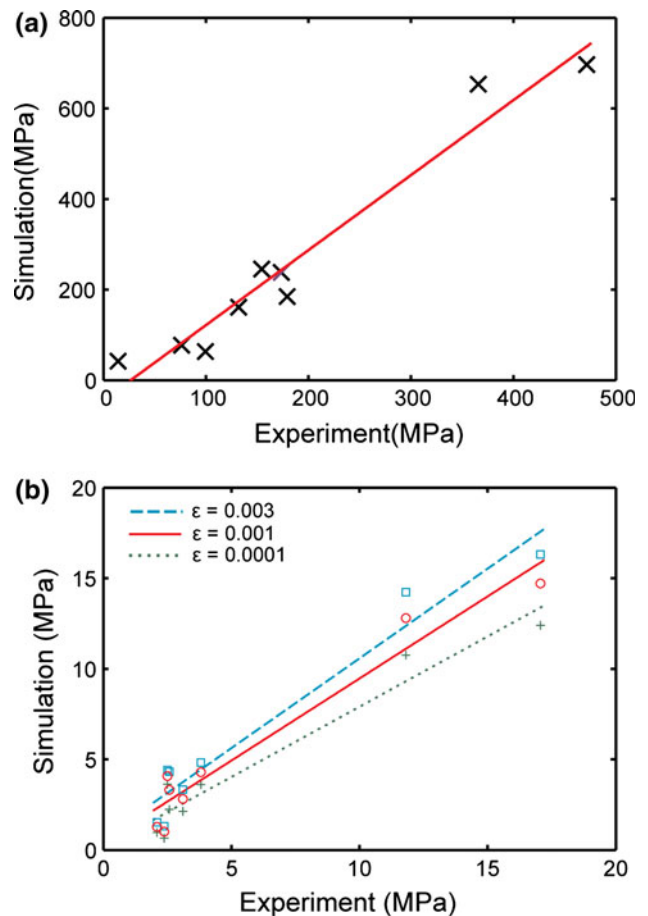


Fig. 8 The relations between the simulated moduli and the experimental moduli of the fabricated scaffolds (a). The relations between the simulated yield stresses and the experimental yield stresses of the fabricated scaffolds (b). The green plots and fitting line indicates minimum $\epsilon = 0.0001$, and the blue plots and line shows maximum $\epsilon = 0.003$. The red plots and fitting line shows $\epsilon = 0.001$ with the highest R^2 (0.946). (Color figure online)

thicknesses [18]. Our scaffolds were composed of repeating unit cells which have similar diameter and different pore and strut sizes, and porosity. The 50% porous scaffolds had thicker walls than the 70% porous scaffolds which determined the mechanical properties depending on scaffold design.

When fabricating three dimensional porous scaffolds for load bearing applications, it is important that the properties of the fabricated scaffolds match the designed properties their designs. According to the results of our study, there is no a significant difference of the compressive modulus or the yield stress among all directions of both the 70 and 50% porous scaffolds. These results are different than some of previous studies where the scaffolds mechanical properties followed the longitudinal alignments of microtubules [36] or a fabrication technique [55]. The anisotropy of their scaffolds relies on the design architecture, however, our 50 and 70% porous scaffolds had uniform architecture in three

directions (X, Y, Z directions), and were not affected by the anisotropy of the casting process.

The files of the designed scaffolds and the μ -CT images of the fabricated scaffolds were further converted to simulate the mechanical properties of the fabricated scaffolds. The goal of the FE simulation is to predict mechanical properties of scaffolds without destroying the scaffolds [20, 56]. Although some previous studies performed the simulation of designed scaffolds [57, 58], these methods could not represent any potential manufacturing defects within the fabricated scaffolds. In addition, other investigators used geometry based FEM [45] to simulate scaffold designs, which required significant pre-processing time [59]. To solve these limitations, many investigators including our own group have used a voxel-based FE method to directly import CT data and automatically create voxel meshes [59, 60]. Thus, μ -CT and the voxel-based FE analysis techniques were adapted in this study to build computer models representing actual fabricated scaffolds including defects. The voxel-based methods are powerful and allow simulation of large models in short time compared with a geometry based technique.

It is known that linear elements have a stiffer behavior than quadratic elements. In order to get accurate simulation, we used greater than a half million linear voxel elements in each model. In spite of the linear analysis, we applied various loadings to predict yield stress since the modified Weibull distribution of modulus is fit to a distribution of elements at a given stress, not an absolute value of stress. Thus, we are looking at the number of the elements that have a certain stress level. This function will not be linear as shown in Fig. 7b, since it is the number of elements that exist at a given stress, and not the stress in a specific element. In other words, the number of elements at a given stress for a high load may not be linearly proportional to the number of elements at a given stress for a low load.

There have been some concerns that the voxel-based method may possess a certain amount of numerical errors inherent to its digitized modeling. Especially at the boundary, there can be oscillations in the responses or local stress concentrations at the stair-like boundary. To evaluate the accuracy of the digital image-based FE method, Guldberg et al. [61] compared voxel-based solutions to analytical solutions and showed that the error was <5% if a structural member is modeled with 10 voxel elements. They also confirmed oscillatory behavior of the stresses in the voxel-based solution; however, the oscillation was around the exact solution, which allowed filtering technique to minimize the errors. In this study, the smallest strut size of the scaffolds was about 300 μm , and the voxel size was 30 μm . The beam diameter to voxel ratio is 10, which indicates the error is small enough to be negligible,

and the stress concentration was minimized in the simulation by averaging stress values [61].

We first performed FE analysis to obtain the stress distributions and the scaffolds deformations under compression. Combined with the bulk mechanical properties of 50:50 PLGA, the FE analysis could also be used to predict potential yield stress of the designed scaffolds. Although the simulation results of the designed scaffolds showed homogeneous stress distribution patterns, the stress distributions of the fabricated scaffolds were heterogeneous and showed tensile stresses besides compression stresses due to defects.

The predicted compressive moduli of the designed scaffolds were greater than the experimental compressive moduli of the fabricated scaffolds because the designed scaffolds do not contain any defects. Experimental scaffolds were mechanically inferior to the computational image based designs due to defects in the actual material such as microcracks, voids and rough layer boundaries. Using FE models alone based on a perfect design without defects can lead to overestimates of mechanical properties.

To achieve a more accurate prediction of scaffolds mechanical properties, the unique approach of combining post-fabrication imaging (μ -CT) and FEA (Voxel FEM) was performed. This approach allowed to capture significant portion of the material defects in the computational model. Comparison between the experimental values and predicted values proved that our computational analysis correlated well with our experimental data. By introducing ε , a small fraction of voxels were allowed to undergo stresses higher than bulk yield even at the ultimate load. A fabricated porous scaffold may not suffer overall yielding even if it experiences local yield stress. We found that variation of ε causes a variation of the correlation, which implies that there may be an optimal value of ε to detect yield loads of the fabricated scaffolds, and further experiments are needed to find the optimal value. Our results showed that simulation using the μ -CT data had better correlation than the designed scaffolds. Although ideally one would look for a 1 to 1 correlation between computational and experimental results, finding a significant correlation between their results is still very helpful for design purposes, especially if the correlation is conservative. Such a correlation would allow engineers to computationally predict how variations in architecture can affect elastic modulus and yield stress and rapidly examine a large range of architectural designs to determine a range of desired properties that would not be feasible using a purely experimental approach.

Limitations of our fabrication method are defects in the final product from the fabrication process, which include air bubbles and residual hydroxyapatite. Although we successfully fabricated solid cubes, there was unavoidable

air rapped during casting of the polymer into the HA secondary molds [24], where molten PLGA was cast into the HA secondary molds. In addition, during decalcification of HA, PLGA may suffer some degradation due to the acidic solution of the RDO. These limitations may be minimized by modifying the design of the secondary molds or the decalcification method.

The difference between the simulations and the experiments may be explained by several factors during processing of images were processed from μ -CT to FE software. Since the grayscale images of the CT data included some noise and did not show clear boundaries of the scaffolds, some details of the scaffolds may be lost when they were exported to stl files. In addition, the resolutions of the original CT images were reduced due to the memory limitation of the FE software and the computer as well as the voxel representation that may lose some details of the scaffolds shapes. The actual material moduli of the base material that makes the scaffolds may be lower than the moduli input for the base material in the FE model, perhaps due to some degradation of polymer material by the RDO acid.

5 Conclusions

It was demonstrated that indirect SFF technique can be used to fabricate designed scaffolds with interconnected porous architectures directly from image-based design techniques. These fabricated scaffolds could attain moduli and strength values in the range of human trabecular bone. Moreover, μ -CT structural measurements of 50:50 PLGA porous scaffolds showed scaffolds had consistent reliable volume fraction similar to designed volume fraction although some casting defects are still present. Thus, measured scaffold modulus and yield stress within trabecular bone range demonstrates that highly porous interconnected scaffolds can be fabricated with load bearing capacity. The mechanical properties of the scaffolds were also simulated using voxel-based FE methods and the result showed strong correlations between the experiments and simulations for both compressive modulus and yield strength. The use of this nondestructive method to predict modulus and yield stress will allow rapid and rigorous evaluation of scaffold mechanical quality for in vivo applications. With further experimental validation more rigorous prediction may be possible.

Acknowledgments This study was supported by National Institute of Health (NIH) R01 grant AR 053379. We also would like to thank for Prof. John Halloran in Materials Science and Engineering for letting us to use their tube furnace and sintering oven.

References

1. Karageorgiou V, Kaplan D. Porosity of 3D biomaterial scaffolds and osteogenesis. *Biomaterials*. 2005;26:5474–91.
2. Athanasίου KA, Agrawal CM, Barber FA, Burkhart SS. Orthopaedic applications for PLA-PGA biodegradable polymers. *Arthroscopy*. 1998;14:726–37.
3. Hutmacher DW. Scaffold design and fabrication technologies for engineering tissues—state of the art and future perspectives. *J Biomater Sci Polym Ed*. 2001;12:107–24.
4. Hollister SJ. Porous scaffold design for tissue engineering. *Nat Mater*. 2005;4:518–24.
5. Ma PX, Choi JW. Biodegradable polymer scaffolds with well-defined interconnected spherical pore network. *Tissue Eng*. 2001;7:23–33.
6. Murphy WL, Dennis RG, Kileny JL, Mooney DJ. Salt fusion: an approach to improve pore interconnectivity within tissue engineering scaffolds. *Tissue Eng*. 2002;8:43–52.
7. Guan L, Davies JE. Preparation and characterization of a highly macroporous biodegradable composite tissue engineering scaffold. *J Biomed Mater Res A*. 2004;71:480–7.
8. Huang YX, Ren J, Chen C, Ren TB, Zhou XY. Preparation and properties of poly(lactide-co-glycolide) (PLGA)/nano-hydroxyapatite (NHA) scaffolds by thermally induced phase separation and rabbit MSCs culture on scaffolds. *J Biomater Appl*. 2008;22:409–32.
9. Hu Y, Grainger DW, Winn SR, Hollinger JO. Fabrication of poly(alpha-hydroxy acid) foam scaffolds using multiple solvent systems. *J Biomed Mater Res*. 2002;59:563–72.
10. Nam YS, Park TG. Porous biodegradable polymeric scaffolds prepared by thermally induced phase separation. *J Biomed Mater Res*. 1999;47:8–17.
11. Thomson RC, Yaszemski MJ, Powers JM, Mikos AG. Fabrication of biodegradable polymer scaffolds to engineer trabecular bone. *J Biomater Sci Polym Ed*. 1995;7:23–38.
12. Wu L, Zhang H, Zhang J, Ding J. Fabrication of three-dimensional porous scaffolds of complicated shape for tissue engineering. I. Compression molding based on flexible-rigid combined mold. *Tissue Eng*. 2005;11:1105–14.
13. Harris LD, Kim BS, Mooney DJ. Open pore biodegradable matrices formed with gas foaming. *J Biomed Mater Res*. 1998;42:396–402.
14. Thomson RC, Yaszemski MJ, Powers JM, Mikos AG. Hydroxyapatite fiber reinforced poly(alpha-hydroxy ester) foams for bone regeneration. *Biomaterials*. 1998;19:1935–43.
15. Lu HH, El-Amin SF, Scott KD, Laurencin CT. Three-dimensional, bioactive, biodegradable, polymer-bioactive glass composite scaffolds with improved mechanical properties support collagen synthesis and mineralization of human osteoblast-like cells in vitro. *J Biomed Mater Res A*. 2003;64:465–74.
16. Rezwani K, Chen QZ, Blaker JJ, Boccaccini AR. Biodegradable and bioactive porous polymer/inorganic composite scaffolds for bone tissue engineering. *Biomaterials*. 2006;27:3413–31.
17. Karande TS, Ong JL, Agrawal CM. Diffusion in musculoskeletal tissue engineering scaffolds: design issues related to porosity, permeability, architecture, and nutrient mixing. *Ann Biomed Eng*. 2004;32:1728–43.
18. Lee KW, Wang S, Fox BC, Ritman EL, Yaszemski MJ, Lu L. Poly(propylene fumarate) bone tissue engineering scaffold fabrication using stereolithography: effects of resin formulations and laser parameters. *Biomacromolecules*. 2007;8:1077–84.
19. Hollister SJ, Lin CY, Saito E, Lin CY, Schek RD, Taboas JM, Williams JM, Partee B, Flanagan CL, Diggs A, Wilke EN, Van Lenthe GH, Muller R, Wirtz T, Das S, Feinberg SE, Krebsbach

- PH. Engineering craniofacial scaffolds. *Orthod Craniofac Res.* 2005;8:162–73.
20. Williams JM, Adewunmi A, Schek RM, Flanagan CL, Krebsbach PH, Feinberg SE, Hollister SJ, Das S. Bone tissue engineering using polycaprolactone scaffolds fabricated via selective laser sintering. *Biomaterials.* 2005;26:4817–27.
 21. Hutmacher DW, Schantz T, Zein I, Ng KW, Teoh SH, Tan KC. Mechanical properties and cell cultural response of polycaprolactone scaffolds designed and fabricated via fused deposition modeling. *J Biomed Mater Res.* 2001;55:203–16.
 22. Hsu SH, Yen HJ, Tseng CS, Cheng CS, Tsai CL. Evaluation of the growth of chondrocytes and osteoblasts seeded into precision scaffolds fabricated by fused deposition manufacturing. *J Biomed Mater Res B Appl Biomater.* 2007;80:519–27.
 23. Sherwood JK, Riley SL, Palazzolo R, Brown SC, Monkhouse DC, Coates M, Griffith LG, Landeen LK, Ratcliffe A. A three-dimensional osteochondral composite scaffold for articular cartilage repair. *Biomaterials.* 2002;23:4739–51.
 24. Weigel T, Schinkel G, Lendlein A. Design and preparation of polymeric scaffolds for tissue engineering. *Expert Rev Med Devices.* 2006;3:835–51.
 25. Taboas JM, Maddox RD, Krebsbach PH, Hollister SJ. Indirect solid free form fabrication of local and global porous, biomimetic and composite 3D polymer-ceramic scaffolds. *Biomaterials.* 2003;24:181–94.
 26. Chen VJ, Smith LA, Ma PX. Bone regeneration on computer-designed nano-fibrous scaffolds. *Biomaterials.* 2006;27:3973–9.
 27. Lee KW, Wang S, Lu L, Jabbari E, Currier BL, Yaszemski MJ. Fabrication and characterization of poly(propylene fumarate) scaffolds with controlled pore structures using 3-dimensional printing and injection molding. *Tissue Eng.* 2006;12:2801–11.
 28. Liao E, Yaszemski M, Krebsbach P, Hollister S. Tissue-engineered cartilage constructs using composite hyaluronic acid/collagen I hydrogels and designed poly(propylene fumarate) scaffolds. *Tissue Eng.* 2007;13:537–50.
 29. Roosa SM, Kemppainen JM, Moffitt EN, Krebsbach PH, Hollister SJ. The pore size of polycaprolactone scaffolds has limited influence on bone regeneration in an in vivo model. *J Biomed Mater Res A.* 2010;92:359–68.
 30. Lin CY, Schek RM, Mistry AS, Shi X, Mikos AG, Krebsbach PH, Hollister SJ. Functional bone engineering using ex vivo gene therapy and topology-optimized, biodegradable polymer composite scaffolds. *Tissue Eng.* 2005;11:1589–98.
 31. Howk D, Chu TM. Design variables for mechanical properties of bone tissue scaffolds. *Biomed Sci Instrum.* 2006;42:278–83.
 32. Middleton JC, Tipton AJ. Synthetic biodegradable polymers as orthopedic devices. *Biomaterials.* 2000;21:2335–46.
 33. Sosnowski S, Wozniak P, Lewandowska-Szumiel M. Polyester scaffolds with bimodal pore size distribution for tissue engineering. *Macromol Biosci.* 2006;6:425–34.
 34. Wu L, Ding J. In vitro degradation of three-dimensional porous poly(D, L-lactide-co-glycolide) scaffolds for tissue engineering. *Biomaterials.* 2004;25:5821–30.
 35. Kim SS, Sun Park M, Jeon O, Yong Choi C, Kim BS. Poly(lactide-co-glycolide)/hydroxyapatite composite scaffolds for bone tissue engineering. *Biomaterials.* 2006;27:1399–409.
 36. Ma PX, Zhang R. Microtubular architecture of biodegradable polymer scaffolds. *J Biomed Mater Res.* 2001;56:469–77.
 37. Wu L, Ding J. Effects of porosity and pore size on in vitro degradation of three-dimensional porous poly(D, L-lactide-co-glycolide) scaffolds for tissue engineering. *J Biomed Mater Res A.* 2005;75:767–77.
 38. Jiang T, Abdel-Fattah WI, Laurencin CT. In vitro evaluation of chitosan/poly(lactic acid-glycolic acid) sintered microsphere scaffolds for bone tissue engineering. *Biomaterials.* 2006;27:4894–903.
 39. Sun W, Starly B, Darling A, Gomez C. Computer-aided tissue engineering: application to biomimetic modelling and design of tissue scaffolds. *Biotechnol Appl Biochem.* 2004;39:49–58.
 40. Hollister SJ, Levy RA, Chu TM, Halloran JW, Feinberg SE. An image-based approach for designing and manufacturing craniofacial scaffolds. *Int J Oral Maxillofac Surg.* 2000;29:67–71.
 41. Hollister SJ, Maddox RD, Taboas JM. Optimal design and fabrication of scaffolds to mimic tissue properties and satisfy biological constraints. *Biomaterials.* 2002;23:4095–103.
 42. Lin CY, Kikuchi N, Hollister SJ. A novel method for biomaterial scaffold internal architecture design to match bone elastic properties with desired porosity. *J Biomech.* 2004;37:623–36.
 43. Ho ST, Hutmacher DW. A comparison of micro CT with other techniques used in the characterization of scaffolds. *Biomaterials.* 2006;27:1362–76.
 44. van Lenthe GH, Hagenmuller H, Bohner M, Hollister SJ, Meinel L, Muller R. Nondestructive micro-computed tomography for biological imaging and quantification of scaffold-bone interaction in vivo. *Biomaterials.* 2007;28:2479–90.
 45. Charles-Harris M, del Valle S, Hentges E, Bleuet P, Lacroix D, Planell JA. Mechanical and structural characterisation of completely degradable polylactic acid/calcium phosphate glass scaffolds. *Biomaterials.* 2007;28:4429–38.
 46. Lacroix D, Chateau A, Ginebra MP, Planell JA. Micro-finite element models of bone tissue-engineering scaffolds. *Biomaterials.* 2006;27:5326–34.
 47. Duty AO, Oest ME, Guldberg RE. Cyclic mechanical compression increases mineralization of cell-seeded polymer scaffolds in vivo. *J Biomech Eng.* 2007;129:531–9.
 48. Jacques SV, Van Oosterwyck H, Muraru L, Van Cleynenbreugel T, De Smet E, Wevers M, Naert I, Vander Sloten J. Individualised, micro CT-based finite element modelling as a tool for biomechanical analysis related to tissue engineering of bone. *Biomaterials.* 2004;25:1683–96.
 49. Chu TM, Halloran JW, Hollister SJ, Feinberg SE. Hydroxyapatite implants with designed internal architecture. *J Mater Sci Mater Med.* 2001;12:471–8.
 50. Chu TM, Orton DG, Hollister SJ, Feinberg SE, Halloran JW. Mechanical and in vivo performance of hydroxyapatite implants with controlled architectures. *Biomaterials.* 2002;23:1283–93.
 51. Turner CH, Burr DB. Basic biomechanical measurements of bone: a tutorial. *Bone.* 1993;14:595–608.
 52. Athanasiou KA, Zhu C, Lanctot DR, Agrawal CM, Wang X. Fundamentals of biomechanics in tissue engineering of bone. *Tissue Eng.* 2000;6:361–81.
 53. Hutmacher DW, Schantz JT, Lam CX, Tan KC, Lim TC. State of the art and future directions of scaffold-based bone engineering from a biomaterials perspective. *J Tissue Eng Regen Med.* 2007;1:245–60.
 54. Kim JY, Jin GZ, Park IS, Kim JN, Chun SY, Park EK, Kim SY, Yoo J, Kim SH, Rhee JW, Cho DW. Evaluation of SFF-based scaffolds seeded with osteoblasts and HUVECs for use in vivo osteogenesis. *Tissue Eng A.* (in press).
 55. Mathieu LM, Mueller TL, Bourban PE, Pioletti DP, Muller R, Manson JA. Architecture and properties of anisotropic polymer composite scaffolds for bone tissue engineering. *Biomaterials.* 2006;27:905–16.
 56. Alberich-Bayarri A, Moratal D, Ivirico JL, Rodriguez Hernandez JC, Valles-Lluch A, Marti-Bonmati L, Estelles JM, Mano JF, Pradas MM, Ribelles JL, Salmeron-Sanchez M. Microcomputed tomography and microfinite element modeling for evaluating polymer scaffolds architecture and their mechanical properties. *J Biomed Mater Res B Appl Biomater.* 2009;91:191–202.
 57. Diego RB, Estelles JM, Sanz JA, Garcia-Aznar JM, Sanchez MS. Polymer scaffolds with interconnected spherical pores and controlled architecture for tissue engineering: fabrication,

- mechanical properties, and finite element modeling. *J Biomed Mater Res B Appl Biomater.* 2007;81:448–55.
58. Miranda P, Pajares A, Guiberteau F. Finite element modeling as a tool for predicting the fracture behavior of robocast scaffolds. *Acta Biomater.* 2008;4:1715–24.
59. Lengsfeld M, Schmitt J, Alter P, Kaminsky J, Leppek R. Comparison of geometry-based and CT voxel-based finite element modelling and experimental validation. *Med Eng Phys.* 1998;20: 515–22.
60. Hollister SJ, Brennan JM, Kikuchi N. A homogenization sampling procedure for calculating trabecular bone effective stiffness and tissue level stress. *J Biomech.* 1994;27:433–44.
61. Guldberg RE, Hollister SJ, Charras GT. The accuracy of digital image-based finite element models. *J Biomech Eng.* 1998;120: 289–95.